Nanoscale

PAPER

View Article Online
View Journal | View Issue

Cite this: *Nanoscale*, 2022, **14**, 7702

Laser-ablation assisted strain engineering of gold nanoparticles for selective electrochemical CO_2 reduction†

Chao Zhang, ‡[a] Wei Zhang,‡[e] Ferdi Karadas, [d] Jingxiang Low, [b] Ran Long, [b] Changhao Liang,*[c] Jin Wang, [a] Zhengquan Li *[a] and Yujie Xiong *[b]

Strain engineering can endow versatile functions, such as refining d-band center and inducing lattice mismatch, on catalysts for a specific reaction. To this end, effective strain engineering for introducing strain on the catalyst is highly sought in various catalytic applications. Herein, a facile laser ablation in liquid (LAL) strategy is adopted to synthesize gold nanoparticles (Au NPs) with rich compressive strain (Au-LAL) for electrochemical CO_2 reduction. It is demonstrated that the rich compressive strain can greatly promote the electrochemical CO_2 reduction performance of Au, achieving a CO partial current density of 24.9 mA cm^{-2} and a maximum CO faradaic efficiency of 97% at −0.9 V for Au-LAL, while it is only 2.77 mA cm^{-2} and 16.2% for regular Au nanoparticles (Au-A). As revealed by the *in situ* Raman characterization and density functional theory calculations, the presence of compressive strain can induce a unique electronic structure change in Au NPs, significantly up-shifting the d-band center of Au. Such a phenomenon can greatly enhance the adsorption strength of Au NPs toward the key intermediate of CO_2 reduction (*i.e.*, *COOH). More interestingly, we demonstrate that, an important industrial chemical feedstock, syngas, can be obtained by simply mixing Au-LAL with Au-A in a suitable ratio. This work provides a promising method for introducing strain in metal NPs and demonstrates the important role of strain in tuning the performance and selectivity of catalysts.

Received 12th March 2022,
Accepted 18th April 2022

DOI: 10.1039/d2nr01400a

rsc.li/nanoscale

Introduction

The high dependence of industrial development on fossil fuels has caused the rapid depletion of fossil fuel reserves, leading to the energy crisis. In addition, the record-high emission of CO_2 attributed to the increasing combustion of fossil fuels has resulted in severe environmental problems.[1] In this regard, developing cost-effective technologies to convert CO_2 into valuable chemical fuels is a critical endeavor for alleviating the above problem.[2–4] Among various proposed strategies, electrochemical CO_2 reduction, which can ideally utilize clean electricity to drive CO_2 conversion, has attracted tremendous attention from the research community.[5–7] Amidst the development of electrochemical CO_2 reduction, Au catalysts have been regarded as one of the most promising candidates due to their appropriate binding energy for the reaction intermediates (*i.e.*, *CO and *COOH) to promote the production of CO.[8,9] Regardless of the significant advances that have been achieved for Au-based catalysts, their electrochemical CO_2 reduction efficiency remains unsatisfactory and can hardly meet the practical requirements. From this perspective, various strategies have been employed and studied to enhance the electrochemical CO_2 reduction performance of Au-based catalysts, such as morphology control, alloying and surface engineering.[10–16]

Recently, strain engineering has been considered as one of the most promising strategies to improve the performance of electrochemical reactions due to its effectiveness in modulating the physicochemical properties of catalysts.[17,18] In particular, theoretical calculations and experimental studies have indicated that the generated strain can modulate the electronic structure and the d-band center, and induce lattice mismatch

[a]*Key Laboratory of the Ministry of Education for Advanced Catalysis Materials, Zhejiang Normal University, Jinhua, Zhejiang 321004, China. E-mail: zqli@zjnu.edu.cn*
[b]*School of Chemistry and Materials Science, University of Science and Technology of China, Hefei 230026, China. E-mail: yjxiong@ustc.edu.cn*
[c]*Key Laboratory of Materials Physics and Anhui Key Laboratory of Nanomaterials and Nanotechnology, Institute of Solid State Physics, Chinese Academy of Sciences, Hefei 230031, China. E-mail: chliang@issp.ac.cn*
[d]*National Nanotechnology Research Center, and Department of Chemistry, Bilkent University, 06800 Ankara, Turkey*
[e]*Institute for Energy Research, Jiangsu University, Zhenjiang, Jiangsu 212013, China*
†Electronic supplementary information (ESI) available. See DOI: **https://doi.org/10.1039/d2nr01400a**
‡These authors contributed equally to this work.

on the catalysts, which in turn optimizes the binding energy of reaction intermediates and boosts catalytic performance.[19,20] For instance, Huang *et al.* reported that the tensile strain could significantly shift up the d-band center of Pd nanoparticles and enhance their adsorption capability toward *COOH, thereby improving the electrochemical CO_2 reduction performance for CO production.[21] Considering the advantages of strain in electrocatalysis, several strategies have been developed to introduce strain into catalysts, such as constructing core–shell structure, regulating morphology and introducing structural defects.[22–24] Although these methods have successfully introduced strain into catalysts, their complexity and poor reproducibility limit the wide applications. Thus an effective method for strain engineering on catalysts is still lacking.

Given the above situation, the laser ablation in liquid (LAL) technique, which can induce gigantic energy input for materials modification, is a potential solution.[25–29] Herein, we prepare Au nanoparticles (NPs) with rich compressive strain *via* the LAL technique using an Au target. Based on the X-ray diffraction (XRD) and transmission electron microscopy (TEM) characterization studies, we discover that the changes in the surface compressive strain can be clearly observed on the Au NPs. After confirming the viability of the LAL technique in introducing strain on the Au NPs, we employ the prepared Au-LAL for electrochemical CO_2 reduction and use regular Au NPs (Au-A) as a comparison. The strain Au NPs have demonstrated a superior electrochemical activity with a maximum CO faradaic efficiency (FE_{CO}) of 97% at −0.9 V. More interestingly, they display high stability with almost no activity decay after operating in 0.1 M $KHCO_3$ electrolyte for 10 h. According to the theoretical simulation results, such an extraordinary electrochemical performance of the Au-LAL originates from the compressive strain in Au NPs, which shifts up the d-band center of Au, thus optimizing the adsorption of key intermediate (*i.e.*, *COOH). To evaluate the feasibility of using Au NPs for syngas production, we mix the Au-LAL with the Au-A for electrochemical CO_2 reduction and find that the H_2/CO production ratio of the system can be simply tuned by changing the mass ratio of strain Au NPs and pristine Au NPs. Our work demonstrates that the LAL technique is a simple yet effective strategy for strain engineering, opening new opportunities for energy and environmental applications.

Experimental section

Preparation of Au-LAL NPs

The Au-LAL NPs were synthesized by laser-ablating the Au target in deionized water. In a typical procedure, the Au target was first polished with sandpaper to remove its surface oxides, followed by dipping into deionized water and ultrasonically rinsing for 5 min. Then the target was fixed onto a supporter in a vessel that was filled with 15 mL of deionized water, and the depth of the water above the target was around 8 mm. The vessel was rotated at a speed of 10 rpm using a motorized tunable stage. Subsequently, the target was ablated using a laser for 15 min. The Nd:YAG pulse laser was set at a frequency of 10 Hz, wavelength of 1064 nm, single-pulse energy of 200 mJ, pulse width of 7 ns and spot size of 1.5 mm diameter focused on the target. The as-prepared colloids were then mixed with carbon black at an Au loading of 30%. The mixture was centrifuged and finally dried at 60 °C in a vacuum oven. For comparison, the strain-free sample (denoted as Au-A) was prepared by annealing Au-LAL NPs loaded on carbon black at 300 °C in N_2 for 2 h.

Materials characterization

XRD patterns were recorded on a Philips X'Pert Pro Super X-ray diffractometer with Cu-Kα radiation (λ = 1.5418 Å). X-ray photoelectron spectra (XPS) were collected on Thermo ESCALAB 250 using monochromatic Al Kα X-ray (1486.6 eV) as the excitation source. TEM was conducted on a JEOL JEM-2100F field-emission high-resolution transmission electron microscope operated at 200 kV. The element concentration was measured using inductively-coupled plasma mass spectrometry (ICP-MS) on Thermo Scientific Plasma Quad 3.

Electrochemical measurements

All the electrochemical measurements were performed on a CHI 660E electrochemical workstation in an H-cell system using a three-electrode system. A Pt foil and a KCl-saturated Ag/AgCl electrode were used as the counter and reference electrodes, respectively. For the preparation of the working electrode, 10 μL of catalyst ink, which was prepared by dispersing 10 mg of the catalyst in the mixture of 100 μL of Nafion solution (5 wt%) and 900 μL of isopropanol, was dropped onto a glassy carbon electrode (5 mm diameter). The working and counter electrodes were separated by a proton exchange membrane into two compartments. All potentials were calibrated to the potentials *vs.* reversible hydrogen electrode (RHE) using the equation: E (*vs.* RHE) = E (*vs.* Ag/AgCl) + 0.197 V + 0.0591 × pH. The linear sweep voltammetry (LSV) curves were measured in CO_2 and Ar-saturated 0.1 M $KHCO_3$ electrolyte at a scan rate of 10 mV s^{-1}. All the electrochemical measurements were performed at ambient temperature and pressure.

Density functional theory (DFT) calculations

The spin-polarized calculations were performed using the Vienna *ab initio* simulation package (VASP 5.4) code.[30,31] The Perdew–Burke–Ernzerhof (PBE)[32] exchange–correlation functional with a generalized gradient approximation (GGA)[33] was adopted to describe the electronic exchange–correlation energy. The projector augmented wave (PAW) pseudopotentials were chosen to describe ion–electron interactions. A cutoff energy of 500 eV was selected through several testing calculations.[34] During the structural relaxation, the convergence threshold for the residual force and energy was set to 0.01 eV $Å^{-1}$ and 10^{-5} eV, respectively. The long-range van der Waals (vdW) interactions were described using the DFT-D3 method with Becke–Johnson damping.[35] Geometry optimization was considered converged until the maximal residual energy and force were less than 1×10^{-5} eV and 0.01 eV $Å^{-1}$, respectively.

The *k*-point sampling of the Brillouin zone was generated automatically by using the Monkhorst–Pack *k*-point mesh with a 3 × 3 × 1 grid for the structural relaxation of the 3 × 3 × 1 supercell. A vacuum slab exceeding 15 Å was employed in the *z* direction to avoid the interaction between two periodic units.

The Gibbs free energies (ΔG) of each elementary reaction were calculated according to the computational hydrogen electrode (CHE) model proposed by Nørskov *et al.*[36] Similar to the previous theoretical studies,[37,38] the adsorption energies of CO_2RR intermediates on the catalyst were obtained relative to CH_4 (g), H_2O (g) and H_2 (g). The chemical potential of a proton/electron ($H^+ + e^-$) was assumed to be equal to half of the chemical potential of gaseous H_2, defined as follows:

$$\Delta E_{CO_2^*} = E_{CO_2^*} + 4E_{H_2(g)} - 2E_{H_2O(g)} - E_{CH_4(g)} - E_* \quad (1)$$

$$\Delta E_{COOH*} = E_{COOH*} + 7/2\ E_{H_2\ (g)} - 2E_{H_2O\ (g)} - E_{CH_4\ (g)} - E_* \quad (2)$$

$$\Delta E_{CO*} = E_{CO*} + 3E_{H_2\ (g)} - E_{H_2O\ (g)} - E_{CH_4\ (g)} - E_* \quad (3)$$

According to this CHE model, the ΔG value could be determined as follows:

$$\Delta G = \Delta E + \Delta ZPE - T\Delta S \quad (4)$$

where ΔE is the electronic energy difference directly obtained from DFT calculations, ΔZPE and ΔS are the change in zero-point energies (ZPE) and entropy (S) during the reaction, respectively, T is the temperature (T = 298.15 K), and the reaction free energy in the CO_2RR (ΔG_{CO_2RR}) is the reaction free energy of the potential-limiting step. The ZPE and TS for all the intermediates of CO_2 reduction on Au systems were calculated using the following equations:

$$E_{ZPE} = \frac{1}{2}\sum_i h\nu_i \quad (5)$$

$$-TS = K_B T \sum_i \ln\left(1 - e^{-\frac{h\nu_i}{K_B T}}\right) - \sum_i h\nu_i \left(\frac{1}{e^{\frac{h\nu_i}{K_B T}} - 1}\right) \quad (6)$$

where h, ν and K_B represent the Planck constant, vibrational frequencies and the Boltzmann constant, respectively.

Results and discussion

In this work, we aim to prepare strain-engineered Au NPs and elucidate the effect of strain on the electronic and electrochemical properties of Au NPs. Au-LAL is synthesized by laser-ablating the Au target in deionized water (Fig. 1). When the Au target is laser-ablated, the high energy of laser can cause a part of the Au target to transform into unstable high-temperature states (*e.g.*, hot vapor or plasma state). Then these unstable states of Au quench instantly to ambient temperature by the surrounding liquid environment, giving rise to the Au-LAL with rich strain.[39,40] The UV-vis absorption spectrum of the as-prepared Au-LAL colloids presents an obvious absorption peak around 520 nm due to the surface plasmon resonance of Au, demonstrating the formation of Au nanostructures (Fig. S1†). As shown in Fig. 2a, the Au-LAL displays a spherical shape with a mean size of 8.5 nm. In addition, the high-resolution TEM (HRTEM) images in Fig. 2b and S2† reveal that Au-LAL exhibits a wavy lattice structure, which can be observed in randomly selected Au-LAL, indicating the severe atomic arrangement distortion and intensive strain on the Au-LAL. For comparison, after annealing treatment, the spherical morphology is preserved on Au-A with a mean size of 8.86 nm while the wavy lattice structure can hardly be found (Fig. S3 and S4†), suggesting the removal of the lattice strain.

To further confirm the structural properties of the prepared samples, XRD characterization is performed (Fig. S5†). Obviously, both Au-LAL and Au-A demonstrate the pattern of the face-centered cubic Au phase (JCPDS no. 01-1613). Interestingly, the (111) and (200) peaks of the Au-LAL are found to shift toward the higher angle direction in comparison with that of Au-A, implying that the Au-LAL possesses a smaller interplanar spacing than Au-A (Fig. 2c). The decrease in interplanar spacing suggests that Au-LAL has a rich compressive strain on the surface, and the strain can be relieved after the heat treatment. Moreover, Rietveld refinement of the XRD patterns is conducted to further analyze the lattice strain of the prepared samples (Fig. S6†). The compressive strain in Au-LAL NPs is calculated to be 0.93%. After annealing, the lattice constants of the prepared samples increase from

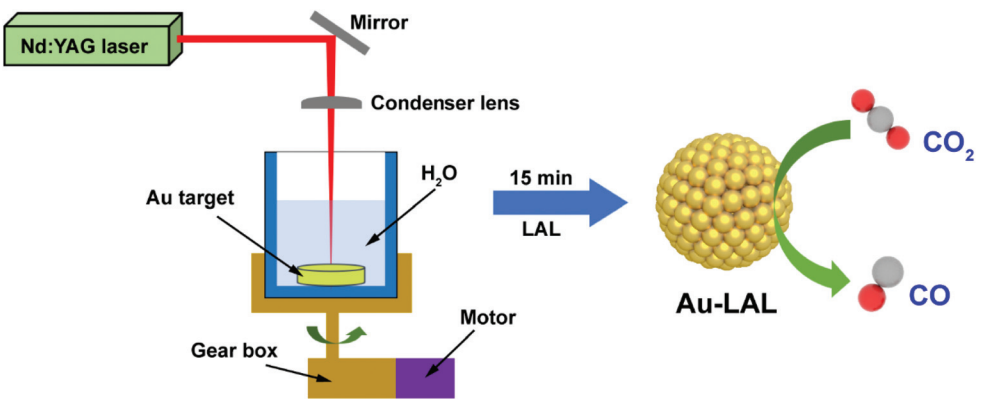

Fig. 1 Schematic illustration of the preparation procedure of Au-LAL for electrochemical CO_2 reduction.

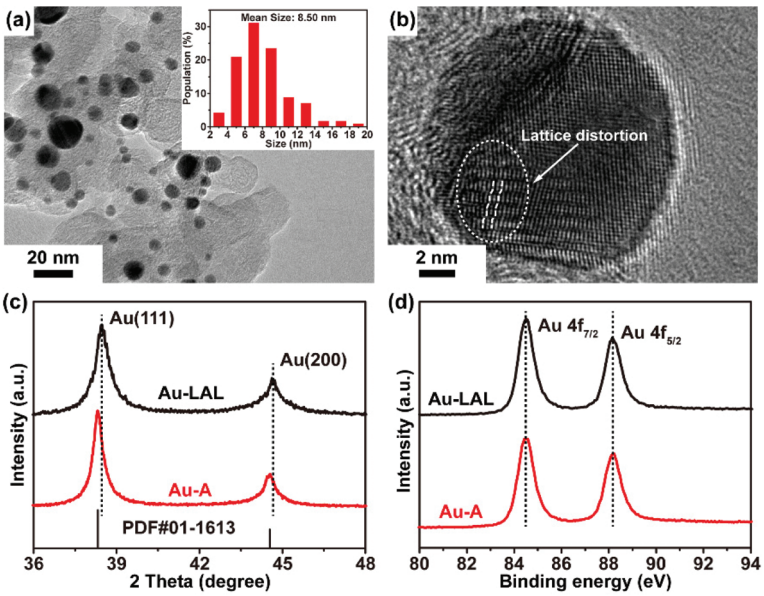

Fig. 2 (a) TEM image of Au-LAL. The inset shows the size distribution of Au-LAL. (b) HRTEM image of an Au-LAL. (c) XRD patterns and (d) high-resolution Au 4f XPS spectra of Au-LAL and Au-A.

4.032 Å to 4.070 Å, indicating the successful removal of the lattice strain on the Au-A *via* heat treatment.

XPS analysis is further carried out to compare the chemical composition and valence states of the prepared sample. Only two peaks at 84.5 and 88.2 eV, which can be respectively attributed to the metallic Au $4f_{2/7}$ and Au $4f_{2/5}$, are observed in the high-resolution Au 4f XPS spectra of both samples (Fig. 2d).[41,42] This confirms that all the prepared samples have a pure chemical composition. Such an inference can also be verified by the high-resolution O 1s spectrum of both samples (Fig. S7b†). Only the peaks attributed to adsorbed H_2O (531.8 eV) and adsorbed oxygen (533.2 eV) can be found, ruling out the possibility of the formation of gold oxides on the prepared samples.[43]

Upon validating the physicochemical properties of the prepared samples, we evaluate their electrochemical CO_2 reduction activity in a typical H-type cell with a CO_2 or Ar-saturated 0.1 M $KHCO_3$ electrolyte. Fig. 3a and Fig. S8† display the LSV curves of the prepared samples. The hydrogen evolution reaction (HER) is the dominant catalytic process starting from −0.6 V when the reaction is performed in an Ar-saturated electrolyte. After purging the electrolyte with CO_2 gas, a significant increase in the current density can be observed, indicating that the CO_2 reduction is more preferable over the HER. Notably, the augmentation of current density in the CO_2-saturated electrolyte with regard to the Ar-saturated electrolyte for Au-LAL is significantly higher than that for the Au-A (Fig. S8†), suggesting the more superior CO_2 reduction performance of the Au-LAL compared to Au-A. In addition, by comparing the LSV curves of the Au-LAL and Au-A, it can be found that Au-LAL shows a higher current density of 25.7 mA cm^{-2} at −0.9 V. Furthermore, the Faraday efficiencies (FEs) of CO_2 reduction products (*i.e.*, H_2 and CO) are determined by gas chromatography (GC). The FEs of different products for Au-LAL and Au-A at different applied potentials are shown in Fig. 3b, Fig. S9 and Table S1.† Prominently, Au-LAL presents the highest selectivity for CO production with FEs over 93% in the potential window from −0.7 to −0.9 V and a maximum FE of 97% at −0.9 V. In contrast, for the Au-A catalyst, the FEs of CO are lower than 20% in the potential range from −0.6 to −1.1 V. Moreover, the partial current density of CO for Au-LAL (24.9 mA cm^{-2}) is far higher than that for Au-A (2.77 mA cm^{-2}) at the applied potential of −0.9 V. Clearly, these results comprehensively show that the Au-LAL has a significantly higher electrochemical CO_2 reduction performance than the Au-A. Interestingly, such an electrochemical CO_2 reduction performance of the prepared Au-LAL also exceeds that of most of the recently reported Au-based electrocatalysts (Table S2†), further confirming the superiority of strain engineering in enhancing the electrocatalytic CO_2 reduction performance of the Au NPs.

Considering the contrasting product distribution of H_2 and CO for Au-LAL and Au-A, the mixture of Au-LAL and Au-A offers an opportunity for the production of syngas. By adjusting the mass ratios of Au-LAL and Au-A from 2 : 1 to 5 : 1, the molar ratios of H_2/CO in syngas change from 2.32 to 0.18 (Fig. S6 and Table S3†). This suggests that the mixture of Au-LAL and Au-A is a promising electrochemical CO_2 reduction catalyst for producing syngas with tunable proportions. Furthermore, a chronoamperometry experiment for Au-LAL is conducted at −0.9 V to evaluate the long-term applicability of the catalysts. As shown in Fig. 3d, the current density and FEs of CO exhibit no distinct decay after electrochemical CO_2 reduction in 0.1 M $KHCO_3$ electrolyte for 10 h, indicating the high stability of Au-LAL. In addition, the XRD and TEM results

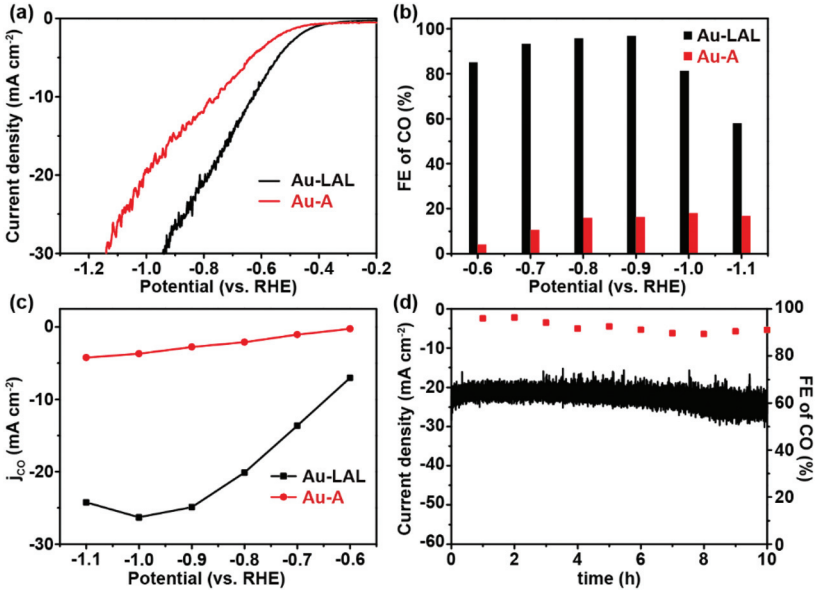

Fig. 3 (a) LSV curves, (b) FEs for electrochemical CO_2 reduction and (c) current density for CO production of Au-LAL and Au-A. (d) Long-term stability test of Au-LAL NPs at −0.9 V *vs.* RHE.

demonstrate that compressive strain and lattice distortion in Au-LAL NPs show negligible changes after the 10 h stability test (Fig. S11 and S12†), further confirming the high durability of the surface strain on the Au-LAL. Taken together, the easily-tuned product distribution and high durability of the prepared catalysts suggest their high practicability.

The information gleaned above has demonstrated that the presence of strain is critical for improving the electrochemical CO_2 reduction performance of the Au NPs. To thoroughly uncover the role of compressive strain in the electrochemical CO_2 reduction toward CO production, we first evaluate the electrochemical surface area (ECSA) of the prepared samples *via* Pb underpotential deposition (Pb-UPD) experiments. As shown in Fig. S13,† the Pb-UPD cyclic voltammetry (CV) curves of both samples display two distinct peaks around 0.45 and 0.61 V attributed to the Au {111} and {110} facets, respectively.[44–46] In addition, a minor difference can be found on the calculated ECSA of the Au-LAL (11.22 cm^2) and Au-A (10.2 cm^2), indicating that the two catalysts have a similar number of active sites. Then we normalize the electrochemical CO_2 reduction performance of the Au-LAL and Au-A for CO production with the obtained ECSAs. As shown in Fig. S14 and Table S4,† the ECSA-normalized partial current density of CO (j_{CO}) of Au-LAL remains overwhelmingly higher than that of the Au-A. Of note, the ECSA-normalized j_{CO} of Au-LAL is 6-fold higher than that of Au-A at an applied potential of −1 V (Fig. S14b†). These results undoubtedly exclude the contribution of the ECSA in enhancing the activity and selectivity of the electrochemical CO_2 reduction of Au-LAL.

Apart from the active site density on the surface, the charge carrier transfer properties of the prepared samples are also determined *via* electrochemical impedance spectroscopy (EIS). The Nyquist plots in Fig. 4a show that Au-LAL possesses a smaller arc diameter than Au-A, suggesting its smaller charge transfer resistance and faster electron transfer across its surface and the electrolyte. Such an enhanced electron transfer rate allows more electrons to participate in the surface reaction, facilitating the reduction reaction on the Au NPs. To deeply explore the reaction kinetics toward CO_2 reduction, the Tafel plots are obtained by utilizing potential *vs.* logarithm of CO partial current density. The Tafel slope of Au-LAL (129.5 mV dec^{-1}) is determined to be far lower than that of the Au-A (159.4 mV dec^{-1}), manifesting the better reaction kinetics of Au-LAL for electrochemical CO_2 reduction to CO.

It is well known that the enhanced reaction kinetics is beneficial for facilitating the CO_2 conversion processes (*e.g.*, intermediate product generation) on the surface of the catalyst. Therefore, we perform *in situ* Raman spectroscopy to track the evolution of surface species on the Au NPs during the electrochemical CO_2 reduction (Fig. S15†). Typically, the Raman spectra are obtained in a range of applied potentials from the open circuit potential (OCP) to −0.5 V. As shown in Fig. 4c and d, two evident peaks can be observed around 1350 and 1650 cm^{-1} attributed to the D-band and G-band of carbon black, respectively.[47,48] For both samples, an obvious peak can be found in the range of 1520–1540 cm^{-1}, assigned to the symmetric stretching vibration of $*CO_2^-$ ($\nu_{as}CO_2^-$) (Fig. 4c and d).[49,50] This peak appears at 0 V *vs.* RHE and its intensity gradually increases with the decrease in the applied potential down to −0.2 V *vs.* RHE. Further decreasing the applied potential from −0.2 to −0.5 V *vs.* RHE, this $*CO_2^-$ intermediate peak gradually decreases and finally disappears at −0.5 V *vs.* RHE, indicating that the $*CO_2^-$ intermediate transforms into other reaction species or desorbs from the Au surface. In particular,

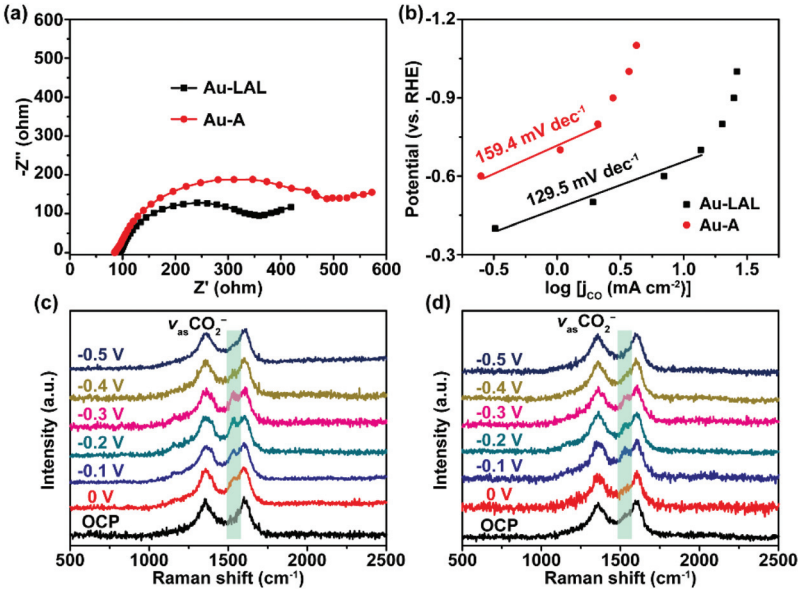

Fig. 4 (a) The Nyquist plots and (b) Tafel plots for the CO production of Au-LAL and Au-A. *In situ* Raman spectra of (c) Au-LAL and (d) Au-A measured in the CO_2-saturated 0.1 M $KHCO_3$ electrolyte at different applied potentials.

by referring to the peak intensity of carbon black, it can be found that this $*CO_2^-$ intermediate peak of Au-LAL is more intense than that of the Au-A, suggesting a relatively higher $*CO_2^-$ coverage on Au-LAL. Clearly, the *in situ* Raman measurements demonstrate that $*CO_2^-$ intermediates can be effectively adsorbed on Au-LAL, thereby promoting the subsequent formation of CO.

Generally, it has been reported that the overpotential of hydroxyl adsorption can be regarded as an indicator for the adsorption strength of $*CO_2^-$ intermediates, and the smaller overpotential indicates the stronger adsorption of $*CO_2^-$ intermediates.[51,52] To further confirm the enhanced adsorption of $*CO_2^-$ on the Au-LAL compared to Au-A, we perform an electrochemical test by investigating the adsorption of OH^- on the prepared samples. As shown in Fig. S16,† the CV curves of the prepared samples are acquired in Ar-saturated 0.1 M $HClO_4$ electrolyte at a scan rate of 20 mV s^{-1}. It is found that the reduction peak of hydroxide Au $(OH)_3$ for Au-LAL displays a negative shift of 15 mV in comparison with that for Au-A. This indicates that the Au-LAL presents stronger adsorption toward $*CO_2^-$ intermediates than Au-A during the CO_2 reduction process.

To have a comprehensive understanding on the function of strain in enhancing the electrochemical performance of Au NPs, we perform DFT calculations on Au catalysts. As shown in Fig. 5a, the 3 × 3 × 1 supercells of Au {111} facets with and without 1% compressive strain are constructed to simulate the Au-LAL and Au-A catalysts, respectively. Considering that the adsorption strength of the key intermediates has a great impact on catalytic activity, we simulate the d-band center (E_d) of metals, which can quantitatively describe the adsorption property of key intermediates on the Au NPs. As shown in Fig. 5b, the E_d of Au {111} facets with and without 1% compressive strain is −1.98 and −2.18 eV, respectively. This suggests that the presence of compressive strain can significantly upshift the E_d of the Au NPs. It should be noted that the position of E_d relative to the Fermi level can be used for evaluating the strength of the metal–adsorbate bond and can be employed as the descriptor for the catalytic activity of the catalysts. The variation in the metal–adsorbate bond is governed by the strength of the coupling between the d-band electrons of the metal and the outmost electrons of the adsorbate. This coupling forms bonding and antibonding states. The bonding states are filled, and the filling of the antibonding states depends on the position of E_d relative to the Fermi level. With the upshift of the E_d, the anti-bonding states can move the Fermi level upward and result in a reduced electron occupation of the anti-bonding orbital, thereby leading to the enhanced adsorption of the reaction intermediates.[31,53] Thus the E_d upshift of Au indicates the enhanced adsorption strength toward the key intermediate of CO_2 reduction on Au-LAL.

Apart from the adsorption capability toward the reactant, we also investigat the influence of strain on the electrochemical CO_2 reduction pathway of the Au NPs. Typically, the reaction pathways of electrochemical CO_2 reduction to CO are considered as four steps (Fig. 5c):[54–56]

$$CO_2\ (g) + * \rightarrow *CO_2 \quad (7)$$

$$*CO_2 + e^- + H^+ \rightarrow *COOH \quad (8)$$

$$*COOH + e^- + H^+ \rightarrow *CO + H_2O \quad (9)$$

$$*CO \rightarrow CO\ (g) + * \quad (10)$$

where * represents the catalytic site. Fig. 5d shows the Gibbs free energy diagrams for CO_2 reduction into CO on Au cata-

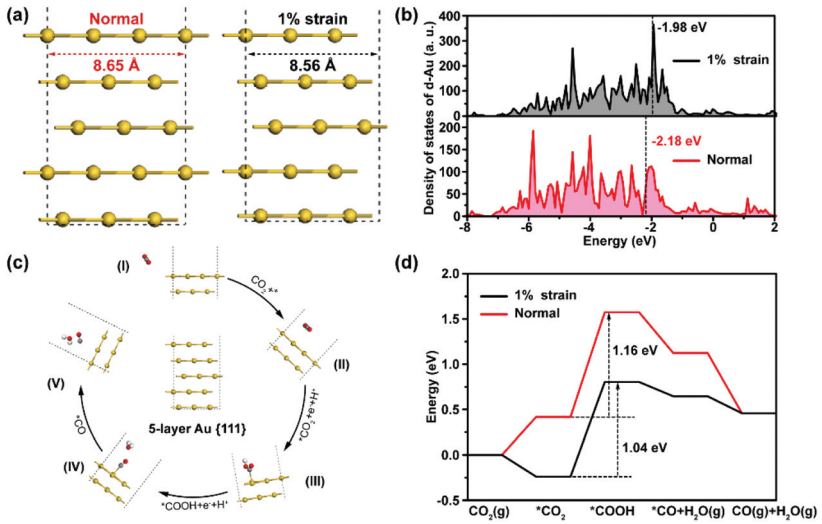

Fig. 5 (a) 3 × 3 Au supercell facets with and without 1% compressive strain. (b) The density of states of Au {111} facets with and without 1% compressive strain. d-band centers are marked with black dotted lines. (c) The proposed reaction pathways of electrochemical CO_2 reduction on Au {111} facets with and without 1% compressive strain. (d) The free energy diagrams of CO_2 reduction to CO for Au {111} facets with and without 1% compressive strain. Yellow, red, white and gray colors indicate gold, oxygen, hydrogen and carbon atoms, respectively.

lysts. Obviously, the formation of the *COOH intermediates is the rate-limiting step for both conditions. Interestingly, the formation of *COOH on Au {111} facets with 1% compressive strain has a lower free energy (1.04 eV) than the pristine Au (1.16 eV). This result is consistent with the E_d upshift of Au caused by the compressive strain, which can more effectively stabilize the rate-limiting *COOH intermediates than the Au without compressive strain, promoting catalytic activity.

Taken together, the experimental and DFT calculation results demonstrate that the compressive strain on the surface of Au can efficiently enhance the electrochemical CO_2 reduction performance of Au-LAL NPs. The compressive strain improves electron transfer between the Au-LAL electrode and electrolyte, allowing more electrons to be involved in the surface reaction and facilitating CO_2 reduction on the Au-LAL NPs. Moreover, the compressive strain in Au NPs upshifts the d-band center, leading to the upward shift of anti-bonding states and a reduced electron occupation of the anti-bonding orbital. As a result, the adsorption of key intermediates on the Au-LAL can be strengthened, boosting the electrochemical CO_2 reduction activity.

Conclusion

In summary, we have prepared Au NPs with rich compressive strain *via* laser ablation of an Au target in water. The prepared Au-LAL displays remarkable electrochemical CO_2 reduction activity with a maximum CO faradaic efficiency of 97% at −0.9 V, which is substantially higher than that of Au NPs without compressive strain (16.2% at −0.9 V). Meanwhile, the catalyst exhibits superior stability with negligible activity deterioration after continuous electrolysis for 10 h. In addition, by mixing the Au-LAL and Au-A at different mass ratios, the molar ratio of H_2/CO can be adjusted in a wide range to obtain the industrial chemical feedstock, syngas. *In situ* Raman and DFT calculations reveal that the excellent electrochemical CO_2 reduction performance originates from the compressive strain, which shifts up the d-band center and thus enhances the adsorption of key intermediates *CO_2 and *COOH. The insights gleaned in this work indicate that laser ablation in liquids is an effective way to introduce strain into metal NPs and afford a new way to construct other high-efficiency catalysts.

Conflicts of interest

The authors declare no competing financial interest.

Acknowledgements

This work was financially supported by the National Key R&D Program of China (2020YFA0406103), the National Natural Science Foundation of China (21701143, 21975223 and 22150610467), the Strategic Priority Research Program of the CAS (XDPB14), the Natural Science Foundation of Zhejiang Province (LGG19B010002 and LZ22B030002), and the Zhejiang Provincial Postdoctoral Program (ZJ2021037).

Notes and references

1 J. D. Shakun, P. U. Clark, F. He, S. A. Marcott, A. C. Mix, Z. Y. Liu, B. Otto-Bliesner, A. Schmittner and E. Bard, *Nature*, 2012, **484**, 49–54.

2 E. V. Kondratenko, G. Mul, J. Baltrusaitis, G. O. Larrazabal and J. Perez-Ramirez, *Energy Environ. Sci.*, 2013, **6**, 3112–3135.
3 M. Robert, *ACS Energy Lett.*, 2016, **1**, 281–282.
4 S. Sultan, J. H. Kim, S. H. Kim, Y. Kwon and J. S. Lee, *J. Energy Chem.*, 2021, **60**, 410–416.
5 F. Bienen, A. Löwe, J. Hildebrand, S. Hertle, D. Schonvogel, D. Kopljar, N. Wagner, E. Klemm and K. A. Friedrich, *J. Energy Chem.*, 2021, **62**, 367–376.
6 P. De Luna, C. Hahn, D. Higgins, S. A. Jaffer, T. F. Jaramillo and E. H. Sargent, *Science*, 2019, **364**, 3506.
7 J. Artz, T. E. Müller, K. Thenert, J. Kleinekorte, R. Meys, A. Sternberg, A. Bardow and W. Leitner, *Chem. Rev.*, 2018, **118**, 434–504.
8 A. Bagger, W. Ju, A. S. Varela, P. Strasser and J. Rossmeisl, *ChemPhysChem*, 2017, **18**, 3266–3273.
9 S. Zhao, R. X. Jin and R. C. Jin, *ACS Energy Lett.*, 2018, **3**, 452–462.
10 S. Li, A. V. Nagarajan, Y. W. Li, D. R. Kauffman, G. Mpourmpakis and R. C. Jin, *Nanoscale*, 2021, **13**, 2333–2337.
11 J. W. Park, W. Choi, J. Noh, W. Park, G. H. Gu, J. Park, Y. Jung and H. Song, *ACS Appl. Mater. Interfaces*, 2022, **14**, 6604–6614.
12 D. Yu, L. Gao, T. Sun, J. Guo, Y. Yuan, J. Zhang, M. Li, X. Li, M. Liu, C. Ma, Q. H. Liu, A. L. Pan, J. L. Yang and H. W. Huang, *Nano Lett.*, 2021, **21**, 1003–1010.
13 S. Li, D. Alfonso, A. V. Nagarajan, S. D. House, J. C. Yang, D. R. Kauffman, G. Mpourmpakis and R. Jin, *ACS Catal.*, 2020, **10**, 12011–12016.
14 M. C. O. Monteiro, M. F. Philips, K. J. P. Schouten and M. T. M. Koper, *Nat. Commun.*, 2021, **12**, 4943.
15 Y. X. Wang, C. Y. Li, Z. X. Fan, Y. Chen, X. Li, L. Cao, C. H. Wang, L. Wang, D. Su, H. Zhang, T. Mueller and C. Wang, *Nano Lett.*, 2020, **20**, 8074–8080.
16 Z. G. Liu, M. N. Hossain, J. L. Wen and A. C. Chen, *Nanoscale*, 2021, **13**, 1155–1163.
17 M. Luo and S. Guo, *Nat. Rev. Mater.*, 2017, **2**, 17059.
18 R. P. Jansonius, L. M. Reid, C. N. Virca and C. P. Berlinguette, *ACS Energy Lett.*, 2019, **4**, 980–986.
19 Z. H. Xia and S. J. Guo, *Chem. Soc. Rev.*, 2019, **48**, 3265–3278.
20 B. You, M. T. Tang, C. Tsai, F. A. Pedersen, X. L. Zheng and H. Li, *Adv. Mater.*, 2019, **31**, 1807001.
21 H. W. Huang, H. H. Jia, Z. Liu, P. F. Gao, J. T. Zhao, Z. L. Luo, J. L. Yang and J. Zeng, *Angew. Chem., Int. Ed.*, 2017, **56**, 3594–3598.
22 K. Su, H. Zhang, S. Qian, J. Li, J. Zhu, Y. Tang and X. Qiu, *ACS Nano*, 2021, **15**, 5178–5188.
23 E. H. Zhang, F. F. Ma, J. Liu, J. Y. Sun, W. X. Chen, H. P. Rong, X. Y. Zhu, J. J. Liu, M. Xu, Z. B. Zhuang, S. L. Chen, Z. H. Wen and J. T. Zhang, *Nanoscale*, 2018, **10**, 21703–21711.
24 B. Schuler, J. H. Lee, C. Kastl, K. A. Cochrane, C. T. Chen, S. Refaely-Abramson, S. Yuan, E. van Veen, R. Roldán, N. J. Borys, R. J. Koch, S. Aloni, A. M. Schwartzberg, D. F. Ogletree, J. B. Neaton and A. Weber-Bargioni, *ACS Nano*, 2019, **13**, 10520–10534.
25 H. B. Zeng, X. W. Du, S. C. Singh, S. A. Kulinich, S. K. Yang, J. P. He and W. P. Cai, *Adv. Funct. Mater.*, 2012, **22**, 1333–1353.
26 J. Xiao, P. Liu, C. X. Wang and G. W. Yang, *Prog. Mater. Sci.*, 2017, **87**, 140–220.
27 R. C. Forsythe, C. P. Cox, M. K. Wilsey and A. M. Müller, *Chem. Rev.*, 2021, **121**, 7568–7637.
28 Q. L. Yuan, S. X. Wei, T. P. Hu, Y. X. Ye, Y. Y. Cai, J. Liu, P. F. Li and C. H. Liang, *J. Phys. Chem. C*, 2021, **125**, 18630–18639.
29 P. Russo, A. Hu, G. Compagnini, W. W. Duley and N. Y. Zhou, *Nanoscale*, 2014, **6**, 2381–2389.
30 G. Kresse and J. Hafner, *Phys. Rev. B: Condens. Matter Mater. Phys.*, 1993, **47**, 558.
31 G. Kresse and J. Furthmüller, *Comput. Mater. Sci.*, 1996, **6**, 15–50.
32 J. P. Perdew, K. Burke and M. Ernzerhof, *Phys. Rev. Lett.*, 1996, **77**, 3865.
33 P. E. Blöchl, *Phys. Rev. B: Condens. Matter Mater. Phys.*, 1994, **50**, 17953.
34 S. Grimme, J. Antony, S. Ehrlich and H. Krieg, *J. Chem. Phys.*, 2010, **132**, 154104.
35 S. Grimme, S. Ehrlich and L. Goerigk, *J. Comput. Chem.*, 2011, **32**, 1456–1465.
36 J. K. Nørskov, J. Rossmeisl, A. Logadottir, L. Lindqvist, J. R. Kitchin, T. Bligaard and H. Jónsson, *J. Phys. Chem. B*, 2004, **108**, 17886–17892.
37 X. Ao, W. Zhang, Z. Li, L. Lv, Y. Ruan, H. H. Wu, W. H. Chiang, C. Wang, M. Liu and X. C. Zeng, *J. Mater. Chem. A*, 2019, **7**, 11792–11801.
38 X. Ao, W. Zhang, Z. Li, J. G. Li, L. Soule, X. Huang, W. H. Chiang, H. M. Chen, C. Wang, M. Liu and X. C. Zeng, *ACS Nano*, 2019, **13**, 11853–11862.
39 D. S. Zhang, B. Gökce and S. Barcikowski, *Chem. Rev.*, 2017, **117**, 3990–4103.
40 J. Y. Lin, C. Xi, Z. Li, Y. Feng, D. Y. Wu, C. K. Dong, P. Yao, H. Liu and X. W. Du, *Chem. Commun.*, 2019, **55**, 3121–3123.
41 X. M. Ma, Y. L. Shen, S. Yao, M. Shu and R. Si, *Chem. – Eur. J.*, 2020, **26**, 4143–4149.
42 A. A. Zhang, J. F. Wu, L. Xue, C. X. Li, S. H. Zeng, D. Caracciolo, S. Wang and C. J. Zhong, *ACS Appl. Mater. Interfaces*, 2021, **13**, 46577–46587.
43 J. Q. Wang, C. Xi, M. Wang, L. Shang, J. Mao, C. K. Dong, H. Liu, S. A. Kulinich and X. W. Du, *ACS Catal.*, 2020, **10**, 12575–12581.
44 Z. Wang, S. Ning, P. Liu, Y. Ding, A. Hirata, T. Fujita and M. Chen, *Adv. Mater.*, 2017, **29**, 1703601.
45 Z. Wang, P. Liu, J. Han, C. Cheng, S. Ning, A. Hirata, T. Fujita and M. Chen, *Nat. Commun.*, 2017, **8**, 1066.
46 X. L. Lu, T. S. Yu, H. L. Wang, L. H. Qian and P. X. Lei, *ACS Catal.*, 2020, **10**, 8860–8869.
47 C. Zhao, S. Zhang, M. Han, X. Zhang, Y. Liu, W. Li, C. Chen, G. Wang, H. Zhang and H. Zhao, *ACS Energy Lett.*, 2019, **4**, 377–383.
48 D. Graf, F. Molitor, K. Ensslin, C. Stampfer, A. Jungen, C. Hierold and L. Wirtz, *Nano Lett.*, 2007, **7**, 238–242.

49 I. V. Chernyshovaa, P. Somasundarana and S. Ponnurangam, *Proc. Natl. Acad. Sci. U. S. A.*, 2018, **115**, E9261–E9270.
50 W. Y. Shan, R. Liu, H. C. Zhao, Z. L. He, Y. J. Lai, S. S. Li, G. Z. He and J. F. Liu, *ACS Nano*, 2020, **14**, 11363–11372.
51 A. Salehi-Khojin, H. R. M. Jhong, B. A. Rosen, W. Zhu, S. Ma, P. J. A. Kenis and R. I. Masel, *J. Phys. Chem. C*, 2013, **117**, 1627–1632.
52 S. Zhang, P. Kang and T. J. Meyer, *J. Am. Chem. Soc.*, 2014, **136**, 1734–1737.
53 J. K. Nørskov, F. Abild-Pedersen, F. Studt and T. Bligaard, *Proc. Natl. Acad. Sci. U. S. A.*, 2011, **108**, 937–943.
54 Q. X. Xie, G. O. Larrazábal, M. Ma, I. Chorkendorff, B. Seger and J. S. Luo, *J. Energy Chem.*, 2021, **63**, 278–284.
55 W. Zhu, R. Michalsky, O. Metin, H. Lv, S. Guo, C. J. Wright, X. Sun, A. A. Peterson and S. Sun, *J. Am. Chem. Soc.*, 2013, **135**, 16833–16836.
56 M. Ma, B. J. Trześniewski, J. Xie and W. A. Smith, *Angew. Chem.*, 2016, **128**, 9900–9904.